Geothermics 105 (2022) 102480

Contents lists available at ScienceDirect

Geothermics

journal homepage: www.elsevier.com/locate/geothermics

Estimation of flow-channel structures with uncertainty quantification: Validation by 3D-printed fractures and field application

Anna Suzuki [a,*], Elvar K. Bjarkason [a], Aoi Yamaguchi [b], Adam J. Hawkins [c], Toshiyuki Hashida [b]

[a] Institute of Fluid Science, Tohoku University, 2-1-1 Katahira, Aoba-ku, Sendai, 980-8577, Miyagi, Japan
[b] Fracture and Reliability Research Institute, Tohoku University, 6-6-11-709, Aza-Aoba, Aramaki, Aobaku, Sendai, 980-8577, Miyagi, Japan
[c] Smith School of Chemical and Biomolecular Engineering, Cornell University, Ithaca, NY, USA

ARTICLE INFO

Keywords:
Injection
Fracture flow
3D printer
Temperature response
Uncertainty quantification

ABSTRACT

Reinjection is an integral part of operating enhanced geothermal systems. Since cooling of reservoirs may occur due to cold-water injection, the possible effects of injection should be assessed. Subsurface structures, especially surface areas of flow channels connecting injection and production wells, determine the onset and rate of thermal breakthrough at a production well caused by reinjection. Previously, a method to estimate the surface area using temperature data was proposed (temperature-based surface area estimation method), which has only been applied to synthetic data from numerical simulation models and field data from geothermal fields with limited structural information available. In this study, we validated the temperature-based surface area estimation method through thermal flow experiments using a 3D-printed fracture network with known structural and physical properties. Based on measured temperature data, the flow-channel surface area was estimated with an approximate Bayesian uncertainty quantification method. The estimated uncertainty bounds were in good agreement with the design of the 3D-printed sample. We also applied the estimation method to field data from a well-studied experimental field. The estimates were consistent with other geophysical observations and previous numerical modeling studies, which had been used previously to probe fluid pathways in the field. It is expected that the thermal response estimation approach validated in this study can be useful for designing reinjection strategies. Furthermore, 3D-printed flow-channel networks may be useful for validating other estimation methods.

1. Introduction

For geothermal operations, reinjection is a standard way of disposing of waste water from power plants and recharging reservoirs (Stefánsson, 1997; Axelsson, 2008; Kaya et al., 2011; Rivera Diaz et al., 2016). A major obstacle is that reinjection can result in cooling of production wells (thermal breakthrough), since it returns water that is colder than the reservoir and thus lowers the temperature in the reservoir (Horne, 1982; Mora and Torres, 2013; Fridleifsson et al., 2006). For sustainable geothermal development, the advantages of maintaining the reservoir pressure and fluid volume through reinjection need to be balanced with the disadvantages of the associated thermal breakthrough.

Tracer testing is a method to characterize fluid flow and can be used to understand the influence of injected water on geothermal reservoirs. A conventional tracer test involves adding a chemically inert solute tracer to injection fluid to track its migration. Many chemical tracer tests have been conducted in geothermal fields (Robinson and Tester, 1984; Rose et al., 2004; Aksoy et al., 2008). Typical solute tracers are used to detect well connectivity (Egert et al., 2020; Rose et al., 2001; Sanjuan et al., 2006), and tracer return curves are used to estimate flow characteristics, such as the recovery ratio, mean residence time, and swept volume (Seymour and Callaghan, 1997; Brown et al., 1999; Egert et al., 2020). Additionally, if a mass transport model is used to analyze the response curves, we can estimate constitutive parameters in the model, such as the mean fluid velocity and the dispersion coefficient (Berkowitz et al., 2006; Hawkins et al., 2017; Suzuki et al., 2015).

Even though a conventional solute tracer test provides such useful information, it is not enough to accurately evaluate the thermal effects associated with the reinjection nor to predict future production temperatures because those tests do not reveal the likely heat exchange between the injected water and the reservoir rocks. The rate of heat exchange is determined by the surface area where the injected water contacts the rocks (Aksoy and Serpen, 2005; Hawkins et al., 2017, 2020). Reactive tracer tests involving adsorbing tracers are a promising

* Corresponding author.
E-mail address: anna.suzuki@tohoku.ac.jp (A. Suzuki).

https://doi.org/10.1016/j.geothermics.2022.102480
Received 4 March 2022; Received in revised form 27 April 2022; Accepted 31 May 2022
0375-6505/© 2022 The Author(s). Published by Elsevier Ltd. This is an open access article under the CC BY license (http://creativecommons.org/licenses/by/4.0/).

emerging approach for flow-channel surface area estimation (Hawkins et al., 2018; Reimus et al., 2020). Recently, Hawkins et al. (2018) and Wu et al. (2021) demonstrated for a mesoscale field injection test that models calibrated using observations from adsorptive tracer tests can provide thermal breakthrough predictions that reflect observed production temperature changes. However, the reliability of this approach has yet to be demonstrated for elevated temperature conditions encountered in geothermal fields.

Shook and Suzuki (2017) proposed using thermal breakthrough responses to estimate surface areas of fluid flow channels between wells in enhanced geothermal systems. We call this method the "temperature-based surface-area estimation method". Shook and Suzuki (2017) used an analytical heat transfer model defined by the rock and fluid properties, and flow conditions. Apart from the surface area between the water and rocks, most of the parameters required by the model can be estimated based on observations of the thermal properties of the reservoir rock and fluid, and conventional tracer testing. Previously, Co and Horne (2011, 2012) also used tracer and thermal response curves to estimate fracture or flow-channel apertures. Ikhwanda et al. (2018) examined the estimation method proposed by Shook and Suzuki (2017) with numerical simulations and showed that the method could provide acceptable errors (within 10%) for the surface area estimates based on initial temperature decline data (when the temperature had declined more than 30% of its maximum future decline). Suzuki et al. (2019a) and Kittilä et al. (2020) applied the temperature-based surface area estimation method to field data. Their estimated flow-channel surface areas were consistent with the sizes of the studied fields. However, comprehensive details about the flow-channel behavior and structures in those fields were not available and only a rough assessment of the estimation method was possible by comparing the surface area estimates with the size of the well field.

Instead of using simulation, Cherubini et al. (2017) and Pastore et al. (2015) conducted heat and tracer transport experiments with a lab-scale fractured rock body consisting of limestone. Their fracture was real, but the fracture's properties could not be fully controlled and reproducible structures could therefore not be used. Suzuki et al. (2017) proposed using 3D-printed fracture models to validate the accuracy of numerical models. The advantage of using a 3D-printed fracture sample is that it allows us to conduct flow experiments using a controllable lab-scale fracture network with a known design and known physical properties (Suzuki et al., 2017, 2019b). In addition, this approach can avoid the numerical errors associated with numerical modeling of heat transfer in complex fracture structures.

In this study, we validated the temperature-based surface-area estimation method proposed by Shook and Suzuki (2017) by analyzing thermal flow experiments conducted using a 3D-printed fracture network. The following section outlines the estimation method that uses a heat-transfer model to estimate flow-channel properties. The approach by Shook and Suzuki (2017) involved calibrating a single model that provides a single point estimate of the surface area. Thus, their approach did not directly quantify the uncertainty or non-uniqueness of their estimates. In the present study, we used an additional approximate Bayesian uncertainty quantification method that takes observation errors and model uncertainty into account. We focused on the ability to estimate the flow-channel surface area and not on future predictions. Thus, the thermal breakthrough analysis considered a long observation period. Because we used 3D-printed fractures with known properties, the designed geometry of the 3D-printed fractures were used to verify the accuracy and applicability of the estimation. After validating the method, we applied the temperature-based surface area estimation method to field data from a well-studied experimental field.

2. Estimation of flow-channel surface area

The estimation approach we consider here uses observed temperature changes associated with reinjection (Shook and Suzuki, 2017). Unlike Shook and Suzuki (2017), who considered using both tracer and temperature data, here we only consider temperature data. We use temperature data to calibrate a heat transfer model, which provides estimates of flow-channel properties, such as flow-channel surface areas. In this section, we introduce the heat transfer models and a method for quantitative evaluation of model parameter uncertainty used in this study.

2.1. Heat transfer models

2.1.1. Basic model

Propagation of a thermal front in a single-phase geothermal system hosted in homogeneous rocks has been studied for several decades. Lauwerier (1955) developed an analytical solution for heat transfer during one-dimensional flow with heat loss to confining beds. Later, Gringarten and Sauty (1975) extended that solution to geothermal problems. Their model assumes that injected water flows along a confined aquifer connecting a pair of injection and production wells. The confined aquifer has a parallel plate geometry and is bounded by impermeable rock. Water is transported along the confined aquifer by advective flow, and the exchange of heat between the fluid and surrounding rock is assumed to be governed by the conductive properties of the rock. Thermal conduction in the direction of the fluid velocity vector is neglected. Assuming that the aquifer is a fracture or flow-channel with a porosity of 1, the governing heat-transport equations of this model are given by

$$\begin{aligned}(\rho C)_w\left(\frac{\partial T_f}{\partial t}+u\frac{\partial T_f}{\partial x}\right)&=\frac{K_R}{b}\frac{\partial T_R}{\partial y}\bigg|_{y=b} \quad , \quad |y|<b\\ (\rho C)_R\frac{\partial T_R}{\partial t}&=K_R\frac{\partial^2 T_R}{\partial y^2} \quad , \quad |y|\geq b \quad .\end{aligned} \tag{1}$$

Here, T_f is the water temperature within the flow channel, T_R is the temperature in the surrounding rock, t is time, x is the coordinate along the flow-channel axis, and y is the coordinate perpendicular to the flow-channel axis. The parameter b represents half of the flow-channel aperture, ρ denotes density, C denotes specific heat capacity, and K_R is the thermal conductivity of the rock. Note that the subscripts w, f, and R are used to indicate values associated with the water, flow channel, and rock, respectively. The mean fluid velocity u is assumed to be constant along the flow channel over time, and the surrounding rock is assumed to extend infinitely away from the flow channel.

For the boundary and initial conditions, we assume that the flow-channel fluid and surrounding rock have a constant initial temperature T_0, and when the injection begins at time $t = 0$, the injection temperature T_I changes instantaneously (in a step-wise fashion) at the flow-channel inlet from the initial temperature T_0 to a constant injection temperature T_I. The resulting analytical solution for the temperature at the flow-channel outlet can be written as (Gringarten and Sauty, 1975)

$$T(t)=T_0-(T_0-T_I)\mathrm{erfc}\left(\frac{\eta A}{2q}\left(t-\frac{V}{q}\right)^{-1/2}\right)H\left(t-\frac{V}{q}\right) \quad . \tag{2}$$

Here, $H(\cdot)$ is the Heaviside step function, and A is the flow-channel surface area through which the fluid in the channel exchanges heat with the surrounding rock. For the narrow rectangular channel assumption that is inherent in (1), the surface area includes the two major sides of the channel and is given by $A = V/b$, where V is the pore volume of the flow-channel. The flow rate along the flow-channel is given by $q = Vu/L$, where L is the length of the flow channel, and $\eta = \sqrt{K_R(\rho C)_R}/(\rho C)_w$ is a thermal parameter that depends on the thermal properties of the fluid and rock.

Assuming that the produced fluid is a combination of reinjected fluid flowing along a single flow-channel and fluid produced at the initial temperature T_0, the production temperature T_p is given by

$$T_\mathrm{p}(t)=T_0-\frac{q_\mathrm{inj}}{q_\mathrm{prod}}F\left(T_0-T(t)\right) \quad , \tag{3}$$

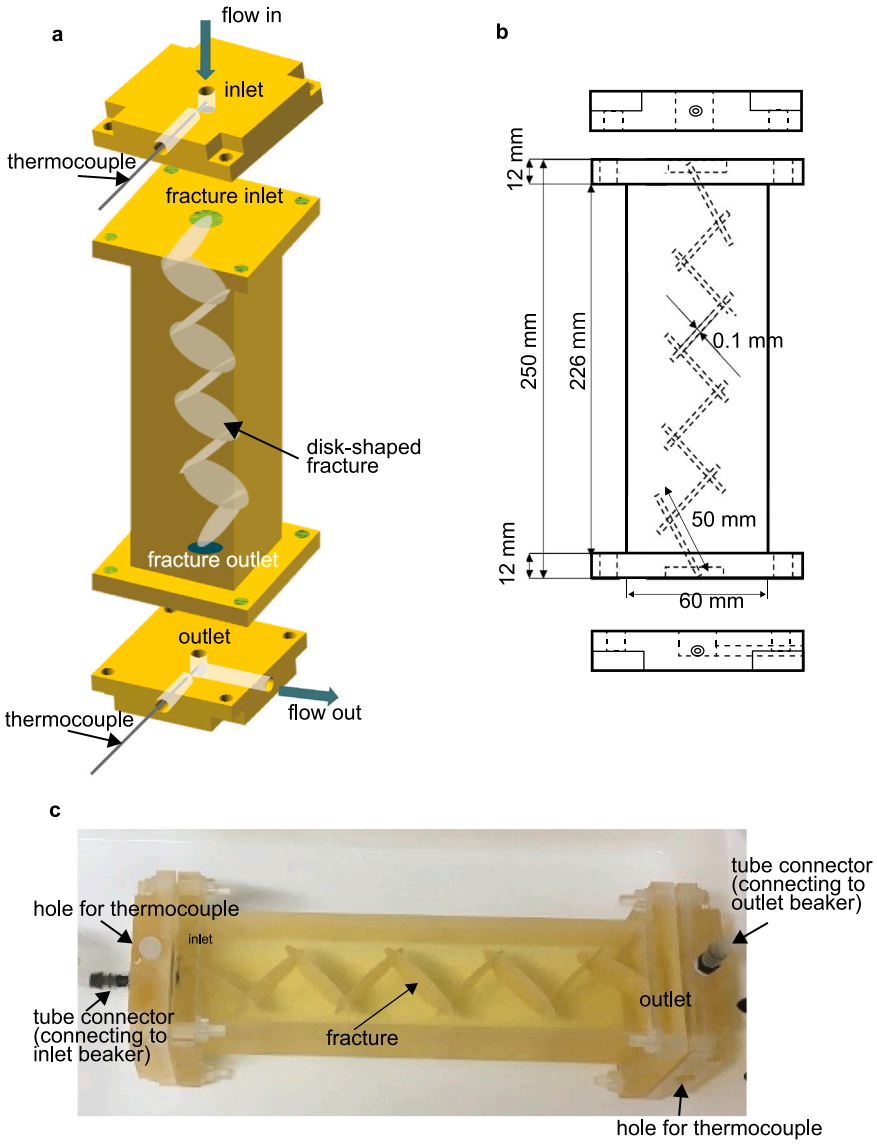

Fig. 1. The 3D-printed fracture sample. (a) Design, (b) blueprint, and (c) photo of the fracture model.

where q_{inj} is the injection rate and q_{prod} is the production rate. The ratio of injected fluid that flows through the flow channel is given by F (that is, $q = Fq_{\text{inj}}$). In this study, we consider the above model as the basic model for heat transfer along a flow channel. This model includes eight parameters $\boldsymbol{p} = [A, V, \eta, T_0, T_I, F, q_{\text{inj}}, q_{\text{prod}}]$. Fig. A.8 in Appendix illustrates the effect that the area and volume parameters have on the basic model.

2.1.2. Extension to multiple flow-channels

Several researchers have used an extension of the basic model (1) in order to describe more diverse flow patterns (e.g., Axelsson et al. (2001), Shook and Suzuki (2017), Suzuki (2017), Suzuki et al. (2019a)). The basic model can be generalized to describe the influence of n flow-channels connecting an injection well and a production well. The generalization commonly used assumes that interactions between different flow-channels can be neglected, and the initial and boundary conditions for each flow-channel are assumed to be the same as the ones used for the basic model. However, it should be noted that ignoring thermal interactions between channels can result in optimistic thermal breakthrough predictions for cases with tightly spaced channels. If we use the subscript i to indicate variables associated with the ith flow-channel connecting the injection well with the production well, then the temperature of the fluid entering the production well through the ith flow channel is described by

$$T_i(t) = T_0 - (T_0 - T_I)\operatorname{erfc}\left(\frac{\eta A_i}{2q_i}\left(t - \frac{V_i}{q_i}\right)^{-1/2}\right) H\left(t - \frac{V_i}{q_i}\right) \quad . \tag{4}$$

Accordingly, the production temperature T_{p} is given by

$$T_{\text{p}}(t) = T_0 - \frac{q_{\text{inj}}}{q_{\text{prod}}} \sum_{i=1}^{n} F_i \left(T_0 - T_i(t)\right) \quad , \tag{5}$$

The ratio of injected fluid that flows through the ith flow-channel is given by F_i (that is, $q_i = F_i q_{\text{inj}}$). When estimating the parameters of more than one flow channel, A_i, V_i, and F_i can differ between the paths, while we assume that T_0, T_I, and η are the same for all paths for simplicity. This solution consists of $3n + 5$ parameters for n flow channels: 3 parameters for each path (A_i, V_i, F_i) and 5 parameters for the entire system ($T_0, T_I, \eta, q_{\text{inj}}, q_{\text{prod}}$). We refer to this solution (5) as the multiple flow-channel model.

Although other finite volume and finite element models can be used to analyze thermal response data (e.g., Hawkins et al., 2017, 2018), the above two models are considerably simpler to use and computationally cheaper, and are therefore commonly used in practice (Aksoy et al.,

2008; Axelsson et al., 2001). Furthermore, a more computationally demanding model does not necessarily result in more reliable results. As Hawkins et al. (2018, 2017) demonstrated using a finite element model, a more computationally demanding model that has an ideal-dipole flow pattern within a 2D fracture of uniform aperture will generally not be flexible enough to match thermal response data nor to reliably predict plausible production temperatures. Later, Hawkins et al. (2020) showed that a finite element model with a nonuniform aperture distribution calibrated based on tracer and pressure data achieved better temperature predictions. Yet, as discussed in Appendix, the basic model provides more variable model outputs than the ideal-dipole model discussed in Hawkins et al. (2018, 2017). Considering this and the additional flexibility afforded by the multiple flow-channel model (5), we consider using the simple analytical models outlined above for estimating uncertainties associated with injection-induced thermal breakthrough.

2.2. Uncertainty quantification

If we can get observations of temperature drawdown caused by water injection, we can compare it with solution (3) or (5) to estimate the surface area of rock that imparts heat to the injected water (Shook and Suzuki, 2017). Shook and Suzuki (2017) considered estimating the surface area by history-matching a single temperature model but did not quantify the uncertainty of the surface area estimation. In this study, we evaluate the uncertainty by considering not only the surface area to be estimated, but also the probability distributions of the other parameters that define the models. In this study, we applied an approximate Bayesian sampling approach called the randomized maximum likelihood (RML) method (Oliver et al., 1996; Oliver, 2017) to estimate model parameter uncertainty.

The RML approach starts by randomly sampling N models (unconditional realizations of model variables) from a prior distribution, which describes what model parameter values $\boldsymbol{p}$ are plausible. Then, the ensemble of N prior models is pushed towards the posterior distribution by solving a nonlinear optimization problem for each candidate model contained in the ensemble. Each optimization problem is a randomized history-matching problem where the observations are corrupted with randomly sampled observation noise. The result is an ensemble of N models, which provide an approximate Bayesian parameter posterior distribution that can be used to describe the model parameter uncertainty given the observations.

The jth RML posterior parameter sample $\boldsymbol{p}_j$ is generated by solving the following nonlinear optimization problem:

$$\boldsymbol{p}_j = \underset{\boldsymbol{p}}{\operatorname{argmin}} \left\{ \left[\boldsymbol{d}(\boldsymbol{p}) - \boldsymbol{d}_{\mathrm{obs},j}\right]^T \Gamma_{\mathrm{d}}^{-1} \left[\boldsymbol{d}(\boldsymbol{p}) - \boldsymbol{d}_{\mathrm{obs},j}\right] + \left[\boldsymbol{p} - \boldsymbol{p}_{\mathrm{uc},j}\right]^T \Gamma_{\mathrm{p}}^{-1} \left[\boldsymbol{p} - \boldsymbol{p}_{\mathrm{uc},j}\right] \right\} \quad . \tag{6}$$

The corresponding prior sample is denoted by $\boldsymbol{p}_{\mathrm{uc},j} \sim \mathcal{N}(\boldsymbol{p}_{\mathrm{pr}}, \Gamma_{\mathrm{p}})$, which is randomly sampled from a multivariate Gaussian prior distribution defined by a prior parameter mean $\boldsymbol{p}_{\mathrm{pr}}$ and covariance matrix Γ_{p}. The stochastic observations are similarly $\boldsymbol{d}_{\mathrm{obs},j} \sim \mathcal{N}(\boldsymbol{d}_{\mathrm{obs}}, \Gamma_{\mathrm{d}})$. For the problem considered in this study, $\boldsymbol{d}_{\mathrm{obs}}$ is a vector of the temperature observations at the production well and Γ_{d} is the covariance matrix of the observation noise, which is assumed to be Gaussian. The simulated temperature observations are denoted by $\boldsymbol{d}(\boldsymbol{p})$. To solve each optimization problem, we used a Trust Region Reflective optimization algorithm that is available in Python's SciPy optimization library.

3. Flow experiments using a 3D fracture model

3.1. Fracture model design and manufacturing

To validate the temperature-based surface area estimation method, we analyzed data from thermal flow experiments carried out using a 3D-printed fracture sample. The fracture sample was designed using the freely available OpenSCAD software (OpenSCAD, 2021). A schematic diagram of the fracture model is shown in Fig. 1. The 3D-printed sample consisted of three sections: two end sections and a main section containing the fractures. The end sections were used for connecting tubes to the inlet and the outlet of the fracture; they also provided additional measurement ports, which could be used for measuring inlet and outlet temperatures. The fracture section consisted of nine intersecting disc-shaped fractures with 50 mm diameters and 0.1 mm apertures. The fractures are depicted in white in Fig. 1a. The fractures overlapped to form a flow-channel from one end of the model to the other end. Although we considered simpler single-fracture models, the zigzagging structure shown in Fig. 1 was chosen considering the model size constraints set by the 3D printer and the need to ensure enough flow-channel surface area to obtain effective temperature data. Based on the 3D-printed design, the effective fracture surface area is expected to be between 0.030–0.035 m^2. The combined surface area of the nine fractures that form the flow-channel was designed to be 0.035 m^2. However, due to the way that the fractures overlap, the effective conductive surface area may be lower (Fig. 1). Discounting the surface areas of the fracture ends that protrude from the fracture intersections gives the lower limit of 0.030 m^2 for the effective surface area.

In this study, we used an ultraviolet curing type 3D printer (Agilista 3100, KEYENCE co.) to generate a 3D-printed sample consisting of acrylic ultraviolet-curing resin. The flow-channel or cavity space was sculpted by the printer with a support material. After 3D printing the sample object, the water-soluble support material was removed to create a clean fracture structure by washing the 3D-printed sample in an ultrasonic bath for several days. A photograph of the 3D-printed fracture sample is shown in Fig. 1c.

3.2. Experimental setup

We used the fracture sample in thermal flow experiments and measured the resulting thermal responses. A diagram and a photo of the experimental setup are shown in Fig. 2. We prepared an inlet beaker at room temperature (around 23 °C) and a heat bath with a heater set to 40 °C. The fracture model was placed in the heat bath as shown in Fig. 2.

To prepare the experiments, the fracture sample was connected with tubes to a pump, an inlet beaker full of water and an outlet beaker as shown in Fig. 2. Before running the flow experiments, the fracture model and flow tubes were saturated with water. This was achieved by pumping water from the inlet beaker through the sample and into the outlet beaker. Subsequently, the pump was turned off and the saturated fracture sample was placed in the heat bath for several hours so that the temperature within the fracture model would equilibrate with that of the heat bath to attain a steady initial temperature T_0.

The analytical heat-transfer models explained in Section 2.1 assume that the inlet temperature changes instantaneously to a constant injection temperature when injection commences. However, for the practical conditions of the experiment, the temperature curve measured at the inlet will not be an ideal step function since flow through the tubes and pathways leading to the inlet will delay and otherwise alter the injection-induced thermal front. To reduce such effects, we used a three-way stopcock in front of the fracture entrance; that allowed us to precool most of the tubing used to connect the fracture with the inlet beaker by circulating injection fluid in front of the fracture entrance until just before injection began. As indicated by the blue arrows in Fig. 2a, the water in the inlet beaker flowed through the pump and was returned to the inlet beaker at the three-way stopcock until the injection experiment started. To start the injection started the three-way stopcock was twisted, and cold water in the inlet beaker was injected into the fracture model (as indicated by the red arrows in Fig. 2a). As a result, we were able to induce the temperature at the

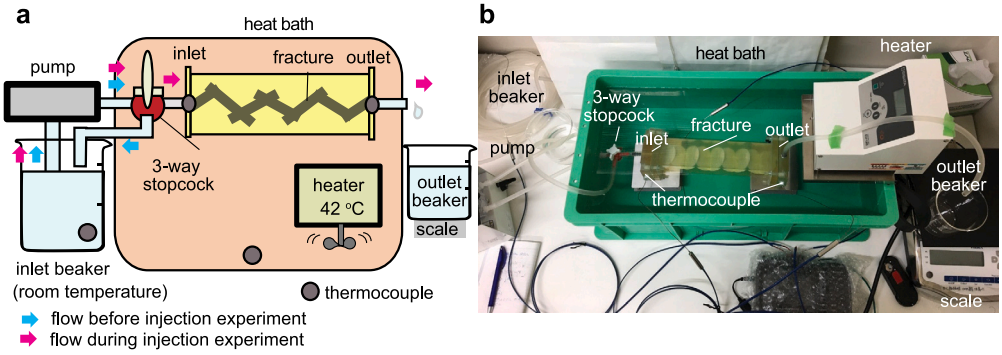

Fig. 2. (a) Schematic of thermal flow experiment involving a 3D-printed fracture sample, and (b) photo of apparatus.

fracture inlet to change relatively abruptly from its initial value to a near constant injection value as shown in Fig. 3.

We carried out the flow experiment four times with constant flow rates of 15, 20, 25, and 30 ml/min. Temperature changes were measured in the inlet beaker, at the fracture inlet, at the fracture outlet, and in the heat bath using K-type thermocouples as shown in Fig. 2. We also used a scale to continuously weigh the mass of produced water that accumulated in the outlet beaker. We used the changes in weighed mass to evaluate the flow rate during each experiment and to confirm that the flow rates were steady and consistent with the rates assigned to the adjustable fluid pump.

3.3. Experimental results

3.3.1. Temperature observations

Observed temperature changes are shown in Fig. 3. Each flow experiment lasted about 11 or 12 min. Temperatures at four locations were logged at two second intervals after injection started. In this study, we used the temperature at the fracture outlet as the production temperature. The measured temperature at the fracture inlet was used to determine the injection temperature and to check whether it was consistent enough with the theoretical assumptions used in the modeling. The temperature of the inlet beaker and the heat bath were also monitored to confirm that they were nearly constant.

Looking at the temperature profiles at the outlet (Fig. 3), a small temperature drop was observed at early times for all flow rates. The arrival time of the initial temperature drop did not appear to correlate systematically with the flow rate so that we considered the initial temperature drop to be caused by some errors from the experimental setup. We thought that we had warmed up the water in the fracture sufficiently before starting the experiment, but perhaps the water in the fracture was not warmed up enough and caused the initial temperature drop. In this study, we considered such effects as measurement errors and used the data as it is. In addition, the temperature in the heat bath was higher than the set value of 40 °C. This may be caused by an error in the heater. However, since the measurement results were almost constant, this was not an issue for the analysis.

3.4. Data analysis

3.4.1. Observations and error model

We analyzed observations from the first 600 s of each experiment. Note that the heat transfer model introduced in Section 2.1 assumes that the surrounding rocks extend infinitely away from the fluid pathway, but the 3D-printed sample has a finite size. Over the 10 min observation period, we expect that the mean distance traveled by a thermal front diffusing into the 3D-printed sample was about $\sqrt{2t\kappa_R} = 1$ cm, where $\kappa_R = K_R/(\rho C)_R$ is the thermal diffusivity of the 3D-printed material. That distance was somewhat smaller than half the diameter of the 6 cm wide main 3D-printed sample containing the fractures. Thus, although the 3D-printed sample had a finite size, we expect that the duration of the observation period was short enough for it to be reasonable to apply the modeling assumptions outlined above.

Based on the measurements of steady heat bath, injection beaker, and inlet temperatures, the temperature measurement error in the lab was at best about 0.1 °C. However, there appeared to be systematic drift with time for some of the temperature observations shown in Fig. 3, and we do not expect the simple model we used to match the early temperature trend measured at the outlet. Thus, a larger observation error may be appropriate when analyzing the lab data to account for both modeling and measurement/experimental errors. For simplicity, we accounted for such errors using a Gaussian error model where the observation errors were assumed to be independent and identically distributed random variables with a 0.5 °C standard deviation. That is, we applied a diagonal observation covariance matrix Γ_d that had diagonal terms set to $(0.5\ °C)^2$. This assumed error model can likely be improved on by taking into account that the early observation errors looked correlated as can be seen in Fig. 4.

3.4.2. Applied heat transfer model

In this experimental setup, all of the injected water flowed along a single flow-channel and was produced at the outlet (i.e., $q = q_{inj}$, $F = 1$). We, therefore, only used the basic model with one flow-channel to analyze the temperature profiles from the laboratory experiments. In addition to the six essential parameters in the basic model, we also included an additional time delay parameter Δt to account for bias in the assumed time of injection at the fracture inlet. Such bias is, for example, a result of the non-negligible volumes in front of the fracture inlet, that delay the arrival of the thermal front to the inlet as can be seen in Fig. 3. Thus, we estimated seven model variables $\boldsymbol{p} = [\log_{10}(A), \log_{10}(V), q_{inj}, \eta, T_0, T_I, \Delta t]$.

3.4.3. Model priors

Table 1 outlines the prior parameter information used for analyzing the experimental results. As indicated in Table 1, we estimated base-ten logarithms of the fracture surface area A and the volume V. We assumed a prior mean of -2 for $\log_{10}(A)$ (equates to a 0.01 m^2 area) with a rather conservative prior standard deviation of 2. This choice had little impact on the estimates of surface area since they were well informed by the temperature observations. For the fracture volume V, we assumed a prior mean of -5 for $\log_{10}(V)$ with a prior standard deviation of 1. This suggests a prior belief that V is about 10 mL (10^{-5} m^3).

The prior means for the initial temperature T_I and the injection temperature T_0 were chosen based on measured values in each experiment, and thus those prior means varied between experiments. The values listed in Table 1 are the ones used for analyzing the 20 ml/min experiment. We used the early temperatures at the outlet to choose the prior mean for T_0, and we assigned it a prior standard deviation of 0.2 °C. Similarly, we used the temperature at the fracture inlet at

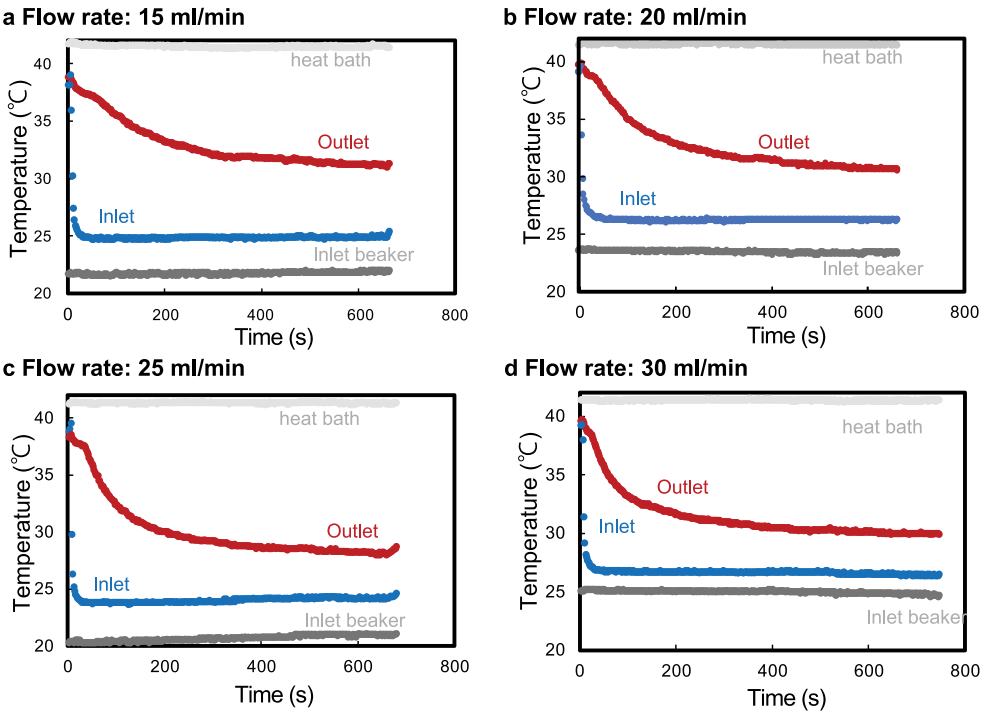

Fig. 3. Temperature data from thermal breakthrough experiments using a 3D-printed fracture sample. The results shown are for injection rates of (a) 15 ml/min, (b) 20 ml/min, (c) 25 ml/min, and (d) 30 ml/min.

Table 1
Model priors and posterior distributions for input parameters in the basic model (3) used to analyze the 3D-printed model experiments. Standard deviations are listed in the columns marked by SD. Physical properties of the Agilista 3100 resin properties were provided by the manufacturer of the 3D printer (KEYENCE co.). Note that the applied prior means for T_0, T_I and q_{inj} were different for each experiment. The example prior values shown here are those that were used for the 20 ml/min experiment.

(a) Prior parameter information

Estimation parameters	Mean	SD
$\log_{10}(A$, surface area [m^2])	−2	2
$\log_{10}(V$, volume [m^3])	−5	1
T_0, initial temperature [°C]	39.8	0.2
T_I, injection temperature [°C]	26.1	1
q_{inj}, injection rate [m^3/s]	20.0	0.5
η, thermal parameter [s$^{-1/2}$ m]	$122 \cdot 10^{-6}$	$1 \cdot 10^{-6}$
Δt, time delay [s]	8	10
Physical properties of water	**Mean**	**SD**
ρ_w, fluid density [kg/m^3]	995	3
C_w, fluid heat capacity [J/(kg K)]	4180	2.5
Physical properties of the resin	**Mean**	**SD**
ρ_R, matrix density [kg/m^3]	1111	11
C_R, matrix heat capacity [J/(kg K)]	1386	14
K_R, thermal conductivity of matrix [W/(m K)]	0.166	0.002

(b) Posterior estimates

Estimation parameters	15 ml/min		20 ml/min		25 ml/min		30 ml/min	
	Mean	SD	Mean	SD	Mean	SD	Mean	SD
$\log_{10}(A$, surface area [m^2])	−1.53	0.03	−1.48	0.02	−1.52	0.02	−1.47	0.02
$\log_{10}(V$, volume [m^3])	−5.9	0.5	−5.6	0.4	−5.1	0.4	−5.6	0.5
T_0, initial temperature [°C]	38.4	0.2	39.4	0.2	38.1	0.1	39.4	0.2
T_I, injection temperature [°C]	27.5	0.4	27.1	0.3	25.5	0.1	27.8	0.2
q_{inj}, injection rate [m^3/s]	15.0	0.5	20.0	0.5	25.0	0.5	30.0	0.5
η, thermal parameter [s$^{-1/2}$ m]	$122 \cdot 10^{-6}$	$1 \cdot 10^{-6}$	$122 \cdot 10^{-6}$	$1 \cdot 10^{-6}$	$122 \cdot 10^{-6}$	$1 \cdot 10^{-6}$	$122 \cdot 10^{-6}$	$1 \cdot 10^{-6}$
Δt, time delay [s]	1	9	4	7	8	9	4	7

late times to determine the prior mean for T_I. Note that, as can be seen in Fig. 3, the observed injection temperature was not constant. Furthermore, the inlet temperatures were higher than those in the beaker, and the initial inlet and outlet temperatures tend to deviate from the heat-bath temperature. From these observations, we do not necessarily expect that the effective injection temperature was the same as the late-time inlet temperature. To account for this, we chose a 1 °C prior standard deviation for the effective inlet/injection temperature.

The prior mean and standard deviation for the injection rate q_{inj} were based on the assigned injection pump rates and measured flow rates by the outlet. The difference between the assigned flow rate and the average measured value was less than 0.1 ml/min. Yet, we assumed a prior standard deviation of 0.5 ml/min based on conservative estimates of transient fluctuations in measured flow rates.

The thermal parameter $\eta = \sqrt{K_R(\rho C)_R}/(\rho C)_w$ depends on the thermal properties of the fluid and rock (in this case the 3D-printed resin). We approximate the prior variance of η by

$$\sigma_\eta^2 = \left(\frac{\partial \eta}{\partial \rho_w}\right)^2 \sigma_{\rho_w}^2 + \left(\frac{\partial \eta}{\partial C_w}\right)^2 \sigma_{C_w}^2 + \left(\frac{\partial \eta}{\partial K_R}\right)^2 \sigma_{K_R}^2 + \left(\frac{\partial \eta}{\partial \rho_R}\right)^2 \sigma_{\rho_R}^2 + \left(\frac{\partial \eta}{\partial C_R}\right)^2 \sigma_{C_R}^2, \quad (7)$$

where σ_s denotes the prior standard deviation of variable s. To reflect the properties of water at the range of experimental temperatures between 20 °C and 40 °C, we assumed for density of water a prior mean of 995 kg/m^3 and a standard deviation σ_{ρ_w} of 3 kg/m^3, and for the heat capacity of water we used a prior mean of 4180 J/(kg K) and a standard deviation σ_{C_w} of 2.5 J/(kg K). The prior mean values for the thermal conductivity, density, and heat capacity of the 3D-printed material were based on values provided by the manufacturer of the 3D printer (KEYENCE co.). The manufacturer did not provide information on the possible errors associated with those reported values. We, therefore, arbitrarily assigned prior standard deviations that equal to 1% of their respective prior mean values. Those values are listed in Table 1. Based on the above, the combined parameter η has a prior mean of 1.22×10^{-4} s$^{-1/2}$ m and a standard deviation $\sigma_\eta = 0.01 \times 10^{-4}$ s$^{-1/2}$ m.

The time delay factor Δt was assigned a prior mean and a standard deviation of 8 s and 10 s, respectively. The prior mean reflects the typical observed onset of temperature decline at the inlet.

3.4.4. Estimation results

In our analysis, we aimed to estimate the surface area of the flow channel in the 3D-printed fracture sample, but we also needed to simultaneously estimate other uncertain parameters. For each of the flow-rate experiments, the seven estimated parameters $\boldsymbol{p} = [\log_{10}(A), \log_{10}(V), q_{\mathrm{inj}}, \eta, T_0, T_I, \Delta t]$ were randomly sampled from their respective prior distributions and 1,000 prior parameter combinations (prior samples) were prepared. Then, we used the RML method to transform those prior samples into 1,000 posterior parameter samples that provide an ensemble of different models that match the temperature observations.

The results of history-matching the experimental data are shown in Fig. 4. Since the results of the RML analysis provide posterior error bounds for the model and its parameters, the figure shows 95% credibility intervals (CIs) for the history-matched model. The results show that the model matches were in good agreement with the experimental observations except for the initial temperature drops. As discussed previously, the initial temperature drops might be due to errors in the experimental setup. The early temperature decline profile was likely caused by a heterogeneous initial temperature distribution resulting from heating up the sample for a length of time that was insufficient for achieving steady and homogeneous initial temperature conditions. The model is unable to reflect such a case since the model assumes a constant and homogeneous initial temperature distribution.

Table 1 presents results of the parameter estimation. It presents the posterior estimates based on estimated means and standard deviations to summarize some of the results of the RML estimation, although the posterior parameter distributions were not necessarily Gaussian. The statistics of the estimated surface areas for each flow rate are shown in Fig. 5. Based on the 3D-printed design, the effective fracture surface area should be between 0.030–0.035 m^2 as discussed previously. The estimated posterior mean values for the surface area ranged between about 0.030 m^2 and 0.034 m^2 for the four flow experiments. Those values and the estimated error bounds were consistent with the design of the 3D-printed fracture sample, as shown in Fig. 5. The four error bars shown in Fig. 5 suggest that the effective surface area controlling the conductive heat transport may be somewhere in the middle of the range indicated by the 3D design or around 0.0325 m^2.

In the same way as we estimated the surface area, we also estimated the other model parameters. The estimates of the mean log-transformed volume ranged between −5.9 and −5.1 (Table 1). That range was consistent with the reference volume of the fracture sample that was designed to be about $1.8 \cdot 10^{-6}$ m^3 (that is, $\log_{10}(V) = -5.7$). Furthermore, the reference volume and each posterior estimate of the mean log-transformed volume agreed within two posterior standard deviations. Likewise, the posterior 95% credibility intervals of the log-transformed volume parameter that were estimated for the four experiments all contained the reference value of the log-transformed volume.

Estimates of the initial temperature T_0, generally, ended up being slightly lower than the earliest temperature observations. This can be seen by comparing the earliest temperature observations in Fig. 4 with the simulated values. This is a result of the models being unable to reproduce the early temperature drop. Moreover, the estimated posterior mean values of the injection temperature T_I were all about 1 °C or 1.5 °C above their respective observed late-time steady inlet temperature. Nevertheless, this is consistent with the observed trend that the minimum breakthrough temperature tended to increase away from the inlet beaker, as can be seen by comparing the temperature observations for the inlet beaker and the fracture inlet (Fig. 3).

The posterior distributions of the thermal parameter η and the flow-rate q_{inj} did not differ from their prior distributions. This is because those parameters were well constrained a priori, while other parameters (most notably, the surface area) were less constrained a priori and the estimation process predominantly involved updating the more uncertain variables. The posterior mean for the time delay factor Δt tended to be somewhat lower than its prior mean that was chosen based on the inlet temperature data. This is a result of the automated calibration procedure having to reject large, positive time delay factors to match the early temperature drop.

These results demonstrated that we can reliably estimate the surface area of a fractured flow channel in a controlled thermal flow experiment. Furthermore, by applying a Bayesian approach, we could quantify the estimation uncertainty for various model parameters, including those describing physical characteristics, such as flow-channel surface area and volume.

4. Field application

In the previous section, we showed that we could reasonably estimate the surface area of a 3D-printed flow channel in a controlled laboratory setting. In this section, we demonstrate how the same approach can be used for actual fields. In most fields, exact flow behavior and flow-channel structures in the underground are unknown, unlike the laboratory experiments. To demonstrate the methodology considered in this study, we used the results of thermal flow tests conducted at the Altona Flat Rocks experimental field, which has been studied extensively over recent years (Hawkins et al., 2018; Tsoflias and Becker, 2008; Tsoflias et al., 2015; Castagna et al., 2011), and compared our results with results from previous studies.

4.1. Outline of field test

The Altona Flat Rocks field is located about 6 km northwest of West Chazy in northern New York State, USA (Hawkins et al., 2017). Several flow studies and tracer tests have been conducted at this experimental field since wells were initially drilled there in 2004. Fig. 6a (Hawkins et al., 2020) presents a schematic image of the Altona Flat Rocks experimental field. It is known that there is a subhorizontal bedding plane fracture that controls the flow at the site. The wells form a five-spot well pattern and they penetrate the conductive subhorizontal

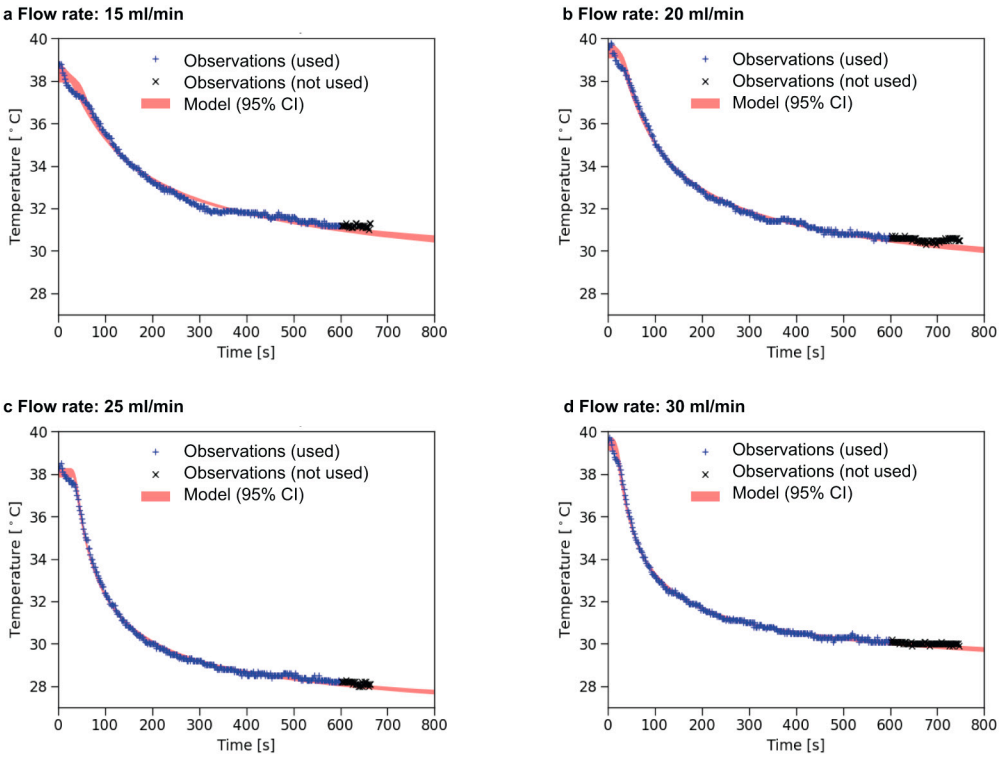

Fig. 4. Model matches to temperature data for the 3D-printed fracture experiments at flow rates of (a) 15 ml/min, (b) 20 ml/min, (c) 25 ml/min, and (d) 30 ml/min.

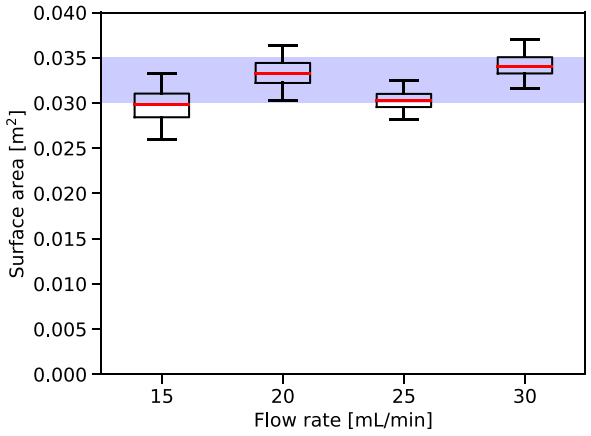

Fig. 5. Estimated fracture surface area for different flow rates. The uncertainty in the surface area estimates is illustrated using boxplots, where the upper and lower ends of each boxplot indicate the 95% credibility interval, the red line shows the median, and the black rectangle indicates the first and third quartiles. The blue region highlights the expected range for the effective surface area based on the design of the 3D-printed fracture sample. (For interpretation of the references to color in this figure legend, the reader is referred to the web version of this article.)

fracture 7.6 m below the surface. Well 204 was used to inject water, and 14.1 m away well 304 was used to produce water from the fracture.

Fig. 6b shows, for another Altona flow experiment, a Ground Penetrating Radar (GPR) survey map of the change in observed amplitude reflections, for the depth of the fracture plane, caused by injection of a saline fluid into the fracture (Hawkins et al., 2018). Note that saline fluid was circulated from wells 304 to 204, which is reverse to the flow direction in the thermal test. The amplitude is a function of the fracture aperture and the salinity of the fluid in the fracture (Tsoflias and Becker, 2008). The change in GPR signal induced by the saline fluid was mainly confined to a narrow region between wells 204 and 304 (Fig. 6b). Therefore, the observed amplitude change indicates that there may be a narrow (1 m to 2 m wide), permeable flow-channel between wells 204 and 304. Fig. 6c shows an example fracture aperture distribution that Hawkins et al. (2020) estimated based on tracer data and observed frictional pressure losses. Their results also suggest that there is a narrow preferential flow-channel between the injection and production wells.

The thermal flow experiment was carried out at injection and production rates of 5.7 L/min with a total volume circulated of 49,250 L (Hawkins et al., 2017). Since the field has a low underground temperature (11.7 °C) at shallow depths, the experiment involved injecting hot water (74 °C) through the injection well 204 and into the subhorizontal fracture (Fig. 6). Fluid circulation was carried out prior to hot water injection between well 204 and well 304 to achieve steady flow conditions. After production, produced water was circulated through a water heater to warm it up to 74°C prior to it being reinjected. The thermal flow experiment lasted 6 days. During the experiment, the production temperature was logged at two minute intervals.

4.2. Data analysis

4.2.1. Observations and error model

We used observations from the first 140 h of the heat exchange experiment, trimmed the observations and only examined temperature observations taken every 30 min. As was the case for the laboratory experiment, we expected that the duration of the experiment was short enough to be consistent with the infinite medium assumptions used in the heat-transfer models. Based on the rock properties reported by Hawkins et al. (2017), a thermal front diffusing into the rock surrounding the fracture can be estimated to travel about 2 m ($\sqrt{2tK_R/(\rho C)_R}$) over the duration of the experiment. This was roughly 5.5 m smaller than the depth of the subhorizontal fracture. Thus, the limited depth of the rock above the subhorizontal fracture was not expected to result in an apparent discrepancy with the models over the

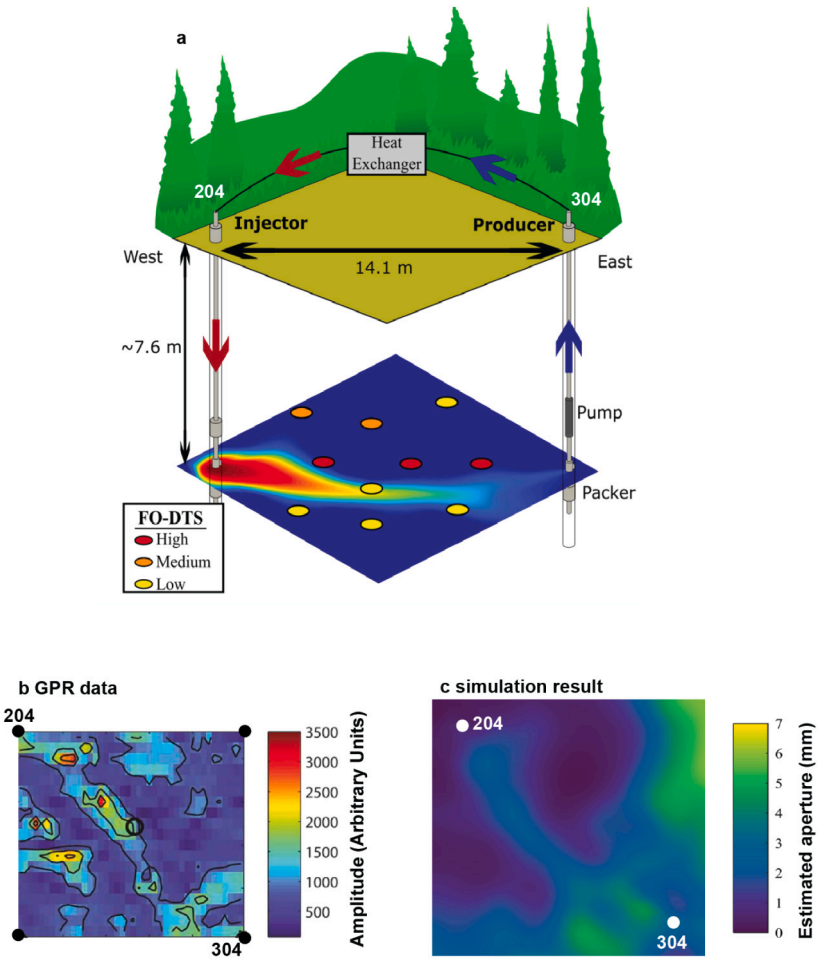

Fig. 6. Overview of the Altona experimental field. (a) Schematic image of the field showing fiber-optic distributed temperature sensing (FO-DTS) measurement locations (Hawkins et al., 2020). The temperature changes at the end of the 6 h injection test are categorized as being high (20 °C or above), medium (around 10 °C), or low (0–5 °C) (Hawkins et al., 2017). The colored contour map shows example simulated temperatures after a day (from Hawkins et al., 2020), where dark blue indicates the initial temperature and dark red indicates the injection temperature. (b) Spatial distribution of amplitude reflections from GPR (Ground Penetrating Radar) survey results after subtracting the background signal (from Hawkins et al., 2018). (c) Estimated fracture aperture distribution based on tracer data (from Hawkins et al., 2020). (For interpretation of the references to color in this figure legend, the reader is referred to the web version of this article.)

observation period. Fiber-optic distributed temperature sensing (FO-DTS) measurements reported in Hawkins et al. (2017) confirm that this assumption is reasonable.

Based on the observed fluctuations in the temperature data, it appears to be reasonable to assign a 0.1 °C standard deviation to the observation error. Yet, we chose a more conservative 0.5 °C standard deviation and assumed the same Gaussian observation error model as we used when analyzing the laboratory experiments.

4.2.2. Applied heat transfer models

Although the 3D-printed sample discussed in the previous section was certain to have only a single flow channel, complex structures in fields may lead to multiple flow channels. Hawkins et al. (2018) observed that the flow behavior at the Altona site was channelized and they were able to account for observed tracer returns using a model with two flow channels. Therefore, we considered modeling heat transfer at the Altona site not only using the basic model (Section 2.1) but also the multiple flow-channel model including two flow channels (Section 2.2).

Unlike the simple modeling used for the laboratory setting, in the field only a fraction of injected fluid may be retrieved at the production well. As a result, we needed to estimate an additional recovery factor (F_i) for each of the modeled flow channels connecting the injection and production wells.

In the previous section, we considered a time delay parameter Δt when analyzing the experimental data because the volume of the injection pipelines in front of the fracture model were not negligible and it could be valuable to introduce a bias-correcting time delay factor to improve the data analysis. In contrast, for the Altona field experiment, the interwell volumes may be large enough relative to the injection volumes connecting the heater with the fracture that we can omit using such a bias-correcting time delay factor. Therefore, in order to reduce the time spent on optimization, the parameter Δt was neglected in the Altona analysis. In addition, it should be noted, that the time delay factor affects the volume estimation but not the surface area estimation, which is the main focus of this study.

4.2.3. Model priors

Table 2 outlines the prior parameter assumptions used for the heat transfer models. Like the analysis for the laboratory experiments, we estimated base-ten logarithms of the flow-channel surface area A and the volume V. Note that the multiple flow-channel model includes two surface areas, volumes, and recovery ratios for the two flow channels, which are denoted by subscripts 1 and 2 (i.e., $A_1, A_2, V_1, V_2, F_1, F_2$). The well field covers an area of about 100 m^2, and based on that we assumed a prior mean of 2 for $\log_{10}(A)$ and a standard deviation of 2. Hawkins et al. (2018) estimated that the total flow-channel volume

Table 2
Altona parameter estimation results for different models. SD indicates the parameter standard deviation, and 95% credibility intervals (CIs) are provided for the posterior estimates.

(a) Basic model

Estimation parameters	Prior		Posterior estimates		
	Mean	SD	Mean	SD	95% CI
$\log_{10}(A$, surface area [m^2])	2	2	1.13	0.06	[1.02, 1.25]
$\log_{10}(V$, volume [m^3])	−1	2	−3.2	0.7	[−5.0, −2.6]
T_0, initial temperature [°C]	11.74	0.10	12.15	0.09	[11.96, 12.32]
T_I, injection temperature [°C]	74	5	73	5	[63, 82]
q_{inj}, injection rate [m^3/s]	$9.5 \cdot 10^{-5}$	$0.1 \cdot 10^{-5}$	$9.5 \cdot 10^{-5}$	$0.1 \cdot 10^{-5}$	$[9.3 \cdot 10^{-5},\ 9.7 \cdot 10^{-5}]$
η, thermal parameter [$s^{-1/2}$ m]	$1.0 \cdot 10^{-3}$	$0.1 \cdot 10^{-3}$	$1.0 \cdot 10^{-3}$	$0.1 \cdot 10^{-3}$	$[0.8 \cdot 10^{-3},\ 1.2 \cdot 10^{-3}]$
F, recovery ratio	0.6	0.2	0.38	0.03	[0.33, 0.46]

(b) Multiple flow-channel model with 2 paths

Estimation parameters	Prior		Posterior estimates		
	Mean	SD	Mean	SD	95% CI
$\log_{10}(A_1$, surface area [m^2])	2	2	0.76	0.14	[0.53, 1.17]
$\log_{10}(V_1$, volume [m^3])	−1	2	−2.5	0.9	[−4.9, −1.3]
T_0, initial temperature [°C]	11.74	0.10	11.76	0.10	[11.57, 11.95]
T_I, injection temperature [°C]	74	5	72	5	[63, 83]
q_{inj}, injection rate [m^3/s]	$9.5 \cdot 10^{-5}$	$0.1 \cdot 10^{-5}$	$9.5 \cdot 10^{-5}$	$0.1 \cdot 10^{-5}$	$[9.3 \cdot 10^{-5},\ 9.7 \cdot 10^{-5}]$
η, thermal parameter [$s^{-1/2}$ m]	$1.0 \cdot 10^{-3}$	$0.1 \cdot 10^{-3}$	$1.0 \cdot 10^{-3}$	$0.1 \cdot 10^{-3}$	$[0.8 \cdot 10^{-3},\ 1.2 \cdot 10^{-3}]$
F_1, recovery ratio	0.4	0.1	0.24	0.03	[0.18, 0.31]
$\log_{10}(A_2$, surface area [m^2])	2	2	1.10	0.15	[0.59, 1.28]
$\log_{10}(V_2$, volume [m^3])	−1	2	−1.6	1.2	[−4.9, −0.2]
F_2, recovery ratio	0.2	0.1	0.20	0.03	[0.15, 0.26]

connecting the wells (that is, the sum of the first and second flow-channel volumes) was about 0.28 m^3 using inert tracer test results. We assumed a prior mean of −1 for $\log_{10}(V)$ with a prior standard deviation of 2. For the multiple flow-channel model, the same prior means and standard deviations were used for the log-transformed area and volume parameters of the first and second flow channels.

A suitable prior mean for the initial temperature T_0 appears to be about 11.74 ± 0.02 °C based on (Hawkins et al., 2017). However, based on the observation noise, we applied a prior standard deviation of 0.1 °C. The injection temperature T_I was 74 ± 2 °C (Hawkins et al., 2017), but since the effective injection temperature at the injection zone might be lower than the injection temperature at the surface, we used a larger prior standard deviation of 5 °C for T_I.

The prior mean for the recovery ratio F was set to 0.6 for the basic model, and the prior standard deviation for the recovery ratio was set to 0.2 to reflect a wide range of a priori plausible values. On the other hand, the multiple flow-channel model used prior means of $F_1 = 0.4$ and $F_2 = 0.2$ for the recovery ratios of the first and second flow channels, respectively. The corresponding prior standard deviations for those recovery ratios were each set to 0.1. The prior mean for the injection rate q_{inj} was chosen based on the flow rate reported by Hawkins et al. (2017, 2018). They did not report any variability in their flow-rate measurements and we arbitrarily assigned a 0.1 m^3/s prior standard deviation for the injection rate. However, this value may understate the error associated with the rate measurements.

Although the physical properties of the flowing water varied with location and time during the test, the models assumed for simplicity that the density and heat capacity of the water was constant. Assuming a representative fluid temperature of around 30 °C, we chose a prior mean of 995 kg/m^3 for the density of water. Its prior standard deviation was chosen as 10 kg/m^3 to roughly reflect the density variability of water at temperatures between 10 °C and 70 °C. For the heat capacity of the water, we chose a prior mean of 4190 J/(kg K) and a standard deviation of 10 J/(kg K) to reflect its variability at temperatures between 10 °C and 70 °C.

Similarly, we represented the uncertainty in the thermal properties of the Altona rock formations, which mainly consist of sandstone. Hawkins et al. (2017) reported that a sample of the Potsdam Sandstone at Altona had a thermal conductivity of 7.6 W/(m K). From Robertson (1988), we can expect conductivities of about 5.0 W/(m K) to 7.5 W/(m K) for sandstone. Therefore, it might be reasonable to use a prior standard deviation of around 1.0 W/(m K). For the mean rock density, we used the 2500 kg/m^3 sandstone density reported by Hawkins et al. (2017), and we assigned it a prior standard deviation of 200 kg/m^3. Hawkins et al. (2017) used a rock specific heat of 930 J/(kg K) based on values reported in Goranson (1942), Robertson (1988). We used the same value for the prior mean and applied a standard deviation of 100 J/(kg K) for the rock specific heat. The employed prior standard deviations for the rock density and specific heat were consistent with values reported for sandstone in the literature (see, e.g., Goranson, 1942; Jacobsen et al., 2003; Geng et al., 2018). Based on the above and Eq. (7), the thermal parameter η was assigned a prior mean of 1.0×10^{-3} $s^{-1/2}$ m and a prior standard deviation of 0.1×10^{-3} $s^{-1/2}$ m.

4.2.4. Surface area estimation

As presented previously for the laboratory experiments, we used the RML method to estimate the uncertainty in the constitutive parameters in each heat transfer model. Figs. 7a, c show the temperature matches using the basic model and the multiple flow-channel model. The resulting estimates of the parameter posterior distributions are listed in Table 2. The multiple flow-channel model provided a good match to the temperature data, while the basic model did not match the data as well. That result was reflected by a biased posterior mean for the initial temperature T_0, which was almost half a degree higher than the observed value (see Table 2).

As before, the estimates for the injection rate q_{inj} and the thermal parameter η did not change from their prior assumptions. However, plausible values for the recovery ratio(s) were narrowed down by the estimation process. The estimates suggested that the observed temperature change might be caused by about 40%–50% of the injected fluid flowing to the production well. This is in agreement with Hawkins et al. (2018). The basic model tended to result in a lower total recovery ratio.

Fig. 7b represents the estimated size of the flow channel in the basic model using an ellipse and compares it with the size of the 100 m^2 well field. The channel is assumed to be horizontal and the ellipse is drawn in such a way that it passes through the injection and production wells. The major axis of the ellipse is aligned with those wells. As defined, the surface area of a horizontal flow-channel includes the top and bottom sides of the channel. However, to visualize the

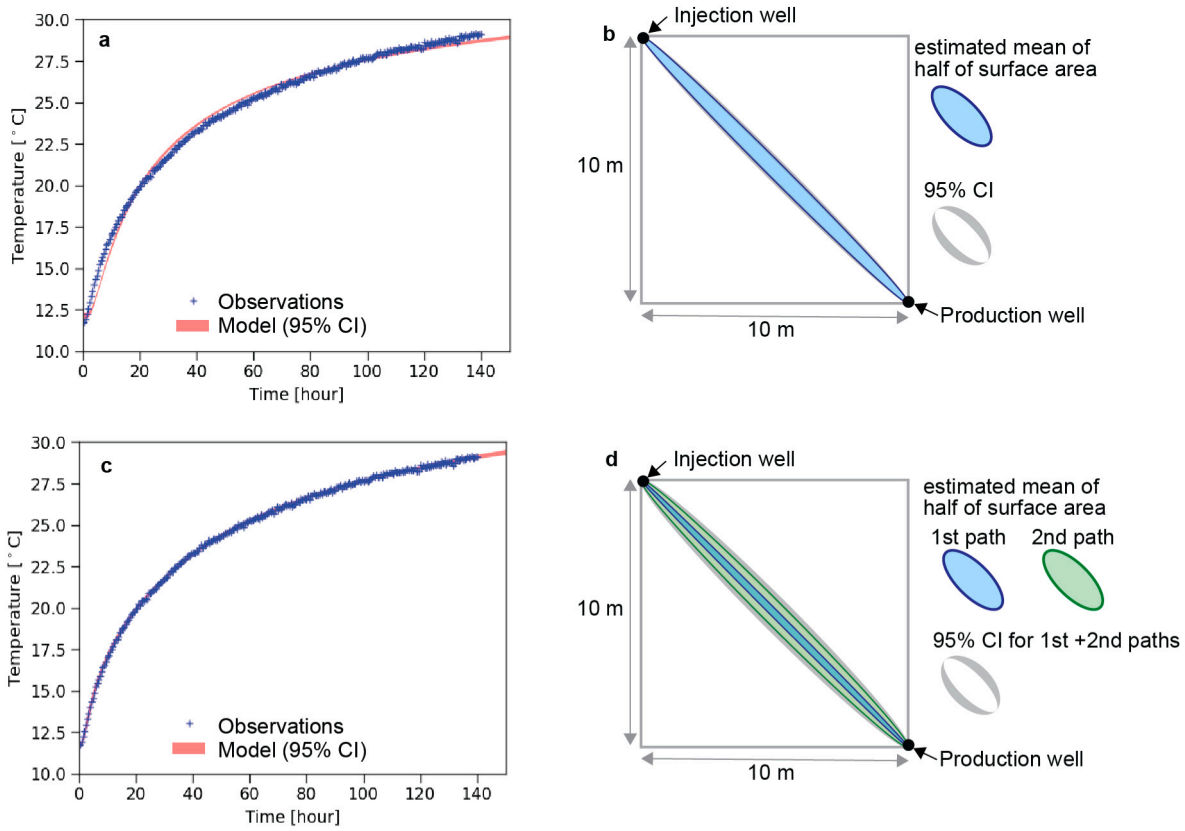

Fig. 7. Surface area estimation results for the Altona experimental field. Results of history-matching the production-well temperatures using (a, b) the basic model and (c, d) the multiple flow-channel model with two paths. The left column compares the temperature observations with the 95% credibility intervals (CIs) of the history-matched models and the right column shows the corresponding estimates of the flow-channel sizes (by depicting half the surface area of each flow channel).

channel size in the horizontal plane, Fig. 7 shows half of the estimated flow-channel surface area. The posterior mean of half the flow-channel surface area is depicted by the blue area, and the 95% credibility interval is represented by the edges of the gray region in Fig. 7b. The basic model estimation indicates that the total flow-channel surface area was about 10.5–17.8 m^2. This result indicates that the water mainly flowed along a narrow path, which was consistent with previous studies on the Altona field (Hawkins et al., 2017, 2018).

The estimated surface areas using the multiple flow-channel model were about 3.4–14.8 m^2 for path 1 and 3.9–19.1 m^2 for path 2. The estimates of the corresponding horizontal cross-sectional areas of those paths are presented in Fig. 7d. The total flow-channel surface area (sum of the flow-channel area of paths 1 and 2) has an estimated 95% credibility interval of 14.3–26.4 m^2, while its posterior mean is about 19.3 m^2. The lower end of this credibility interval overlapped with the upper range of plausible values indicated by the basic model. The two models were thus in reasonable agreement although the multiple flow-channel model indicated a somewhat larger total surface area than the basic model.

4.3. Comparison with previous studies

Based on the elliptical flow-channel depictions in Fig. 7, the flow-channel widths can be estimated to be about 0.6 m for the basic model and 0.9 m for the multiple flow-channel model (for the combination of the two paths). Note that these widths were based on the minor axes of the ellipses shown in Fig. 7b, d. In comparison, Hawkins et al. (2017) presented additional temperature observations from ten passive monitoring wells that indicate that the main flow channel width was less than 4 m (Hawkins et al., 2018). Furthermore, GPR surveys carried out in the field to detect the flow distribution of saline injection fluid (Tsoflias et al., 2015; Hawkins et al., 2017, 2018) provided further constraints on the flow geometry (Fig. 6b) and suggested that the dominant flow channel was roughly 1—2 m wide. Our estimated flow-channel dimensions were consistent with those measurements.

Previously, Hawkins et al. (2018) used results of inert and adsorptive chemical tracers to estimate flow-channel parameters at the Altona site. In their modeling, they assumed two separate flow channels to match the tracer return profiles. Hawkins et al. (2018) estimated that the combined surface area was about 110 m^2 (28 m^2 for path 1 and 80 m^2 for path 2). The estimated total surface area in our two models were in both cases smaller than the total area estimated by Hawkins et al. (2018). The total surface area estimated by the basic and multiple flow-channel models were similar to the 28 m^2 path 1 area estimated by Hawkins et al. (2018).

It should be noted that, in the above uncertainty analysis, we neglected to consider the conceptual uncertainty of how and where the injected fluid that flows to the producer was mixed with other produced fluid that did not originate from the injection. In our modeling, we assumed that the produced fluids were all mixed in the production well and that only injected fluid flowed along each path connecting the injection–production well pair. Hawkins et al. (2018), however, assumed in their modeling that the injected fluid was mixed with additional groundwater near or in the injection well and subsequently the mixed fluid flowed along the paths connected to the production well. The reality is likely some combination of those two extremes and additional mixing of fluids in between the wells. Taking such additional conceptual uncertainty into account will widen the bounds for the surface area estimates—namely, it will increase the upper bound for the surface area. If we reconsider Eqs. (1)–(5) and assume that all the produced fluid flows along a single path, then we can expect the surface area estimate to be $1/F_1$ times higher than our previous estimates

for the basic model. Therefore, the upper bound for the surface area estimated by the basic model, which gave a recovery ratio of about $F_1 = 0.4$, could be increased by a factor of 2.5. That is consistent with what we found when adjusting and rerunning the estimation with the basic model with the modified assumption that all the produced fluid was mixed in the injection well and then flowed along one path to the producer. For that case, the resulting 95% credibility interval was 28.9–44.3 m^2 for the surface area. That range is more compatible with the results of Hawkins et al. (2018) and the area they reported for path 1. This highlights the importance of accounting for conceptual model uncertainty when estimating flow-channel variables. For the problem at hand of estimating the flow-channel surface areas, the conceptual model uncertainty discussed above becomes relatively more significant in cases where the injection contributes to a small proportion of the produced fluid.

We can also compare other parameter estimates with values reported in previous Altona studies, such as flow-channel volumes. Using the results from the inert and adsorptive tracers, Hawkins et al. (2018) estimated that the total flow-channel volume was about 0.28 m^3 (0.08 m^3 for path 1 and 0.20 m^3 for path 2). Our estimated 95% credibility intervals suggest a total volume of about 1.0×10^{-5}–2.5×10^{-3} m^3 for the basic model and 1.2×10^{-3}–0.59 m^3 for the multiple flow-channel model. Although the estimate by the basic model was smaller than the estimate from Hawkins et al. (2018) (even if we assumed that all the produced fluid flowed along a single path connecting the wells and thus increased the volume estimate for the basic model by around a factor of 2.5), the range of the total volume estimates for the multiple flow-channel model agrees with their estimates.

5. Concluding remarks

This study considered a flow-channel surface area estimation method that uses temperature data associated with reinjection. We validated the temperature-based surface area estimation method through thermal flow experiments using a 3D-printed flow-channel model. Because the 3D printer generated flow-channel structures with known geometric properties, we could evaluate the accuracy of the estimation results quantitatively. The observed temperature response curves from the flow experiments were analyzed using simple and fundamental heat transfer models, and the uncertainty was evaluated using an approximate Bayesian sampling approach called the randomized maximum likelihood (RML) method. The results showed that the posterior credibility intervals for the flow-channel surface area estimates were in agreement with the designed flow-channel surface area of the 3D-printed sample.

We also applied the same method to field data from the Altona experimental field. The flow-channel surface area estimation suggested that there was a narrow and preferential flow channel between the injection and production wells at Altona. The estimates indicate that the flow can be attributed to an approximately 1 m wide flow region. This agrees with previous geophysical and simulation studies that suggested that the injected fluid mainly flows along a 1–4 m wide channel (Hawkins et al., 2017, 2018). The estimated total surface area was 10.5–17.8 m^2 for the basic model and 14.3–26.4 m^2 for the multiple flow-channel model. The upper limit of those uncertainty bounds can be increased by about a factor of two by considering the conceptual uncertainty of where the injected fluid mixes with other produced fluid (e.g., in the production well or near the injection well). Those bounds are consistent with the 28 m^2 primary flow-channel surface area estimated by Hawkins et al. (2018) based on an adsorptive chemical tracers test. However, the above bounds do not cover their 80 m^2 surface area estimate for the secondary flow-channel.

Predictions of temperature changes caused by reinjection have typically been based on using one calibrated model. This inevitably results in predictions which are unlikely to adequately reflect the future production response. However, uncertainty quantification methods, such as the one used in this study, are increasingly being used with the aim of improving the reliability of model predictions describing the effects of reinjection in enhanced geothermal systems (Vogt et al., 2012; Wu et al., 2021). Evaluating model uncertainty is easily manageable for the computationally cheap models considered in this study and should be preferred over relying on one calibrated model.

This study used relatively long temperature observation histories to validate the temperature-based surface area estimation method with uncertainty quantification. In practice, the goal would commonly be to provide instructive model predictions before substantial temperature changes occur. Moreover, reinjection is often carried out cautiously because of the fear of cooling and is commonly halted when temperature decline is observed. As a result, practical thermal response predictions need to be made based on relatively short observation histories unlike those considered in this study. According to our previous work (Ikhwanda et al., 2018), a single calibrated model could provide acceptable model estimates of flow-channel surface areas (errors within 10%) when the observed temperature had declined more than 30% of its maximum future decline. On the other hand, by quantifying the model predictive uncertainty, it is possible to evaluate earlier and with less data whether enough information is available to guide operations. Thus, our approach may well be applicable to shorter observation histories, which will be examined in our future research.

The temperature prediction approach considered by Ikhwanda et al. (2018) and Shook and Suzuki (2017) used temperature and non-reactive tracer test observations. Although this study did not consider data from chemical tracer tests, we expect that supplementing temperature observations with additional tracer data is important since tracer observations help to constrain how much injection fluid returns to production wells. As a different approach, chemical tracer testing methods based on reactive tracers, which are sensitive to flow-channel surface areas, and frictional pressure loss observations have shown significant promise as a means for early thermal breakthrough prediction (Hawkins et al., 2020; Wu et al., 2021). At later stages, such tracer observations can also be combined with early thermal breakthrough observations to refine model predictions.

CRediT authorship contribution statement

Anna Suzuki: Conceptualization, Methodology, Validation, Writing – original draft, Visualization, Project administration, Funding acquisition. **Elvar K. Bjarkason:** Methodology, Software, Validation, Formal analysis, Writing – original draft, Writing – review & editing, Visualization. **Aoi Yamaguchi:** Investigation, Data curation. **Adam J. Hawkins:** Resources, Writing – review & editing. **Toshiyuki Hashida:** Writing – review & editing, Supervision.

Declaration of competing interest

The authors declare that they have no known competing financial interests or personal relationships that could have appeared to influence the work reported in this paper.

Acknowledgments

This research was funded by JSPS, Japan KAKENHI Grant Numbers JP20H02676 (Japan) and JST ACT-X Grant Number JPMJAX190H (Japan).

Appendix. Effects of the main parameters in the basic heat-transfer model

Fig. A.8 illustrates how varying either the flow-channel volume or surface area influences the basic temperature model given in Eq. (3). The volume impacts the arrival time or breakthrough of the thermal front but does not alter the shape of the curve after breakthrough. For a

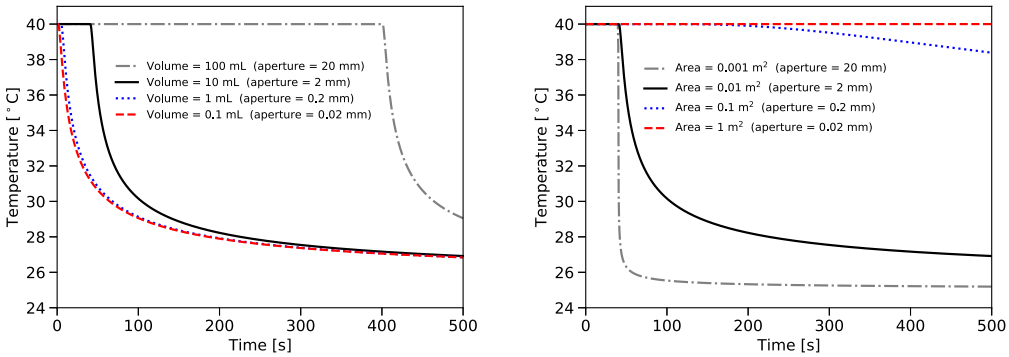

Fig. A.8. Example thermal breakthrough curves for the basic model (3). (Left) The flow-channel volume controls how early thermal breakthrough can occur. However, for small enough volumes, the volume effect on temperature becomes imperceptible and the flow-channel surface area dominates the temperature trend. (Right) The flow-channel surface area determines how rapidly the temperature declines after breakthrough. Model parameters were based on the prior mean values listed in Table 1, while the injection time-delay was set to zero.

fixed volume, the rate of temperature decline decreases with increasing surface area or equivalently with decreasing fracture aperture. This is unlike the uniform aperture fracture model considered by Hawkins et al. (2018, 2017), which has an ideal-dipole flow pattern.

Hawkins et al. (2018, 2017) observed that varying the mean aperture in their ideal-dipole model had a negligible effect on simulated temperatures. The reason is that varying the aperture does not change the effective surface area available for thermal conduction in the ideal-dipole model since the flow pattern is fixed. Instead, the aperture only controls the fracture volume in that model, and the surface area effect overshadowed the volume effect for the realistic range of aperture values considered in Hawkins et al. (2018, 2017). Using the basic model (3), the temperature profiles can vary more with aperture as shown in Fig. A.8.

The derivation of the basic model assumes that the aperture is much smaller than the width of the fracture. However, the model is often applied, in practice, using parameter combinations which are inconsistent with that assumption. For instance, after estimating flow-channel volumes using inert tracer tests, geothermal modelers sometimes generate conservative or pessimistic temperature forecasts by choosing an aperture or a surface area representative of a square or circular flow-channel cross-section (Axelsson et al., 2001, 2005). The resulting forecasts are pessimistic since they are based on adopting a minimal heat-transfer surface area for a given fracture volume and length.

The temperature curves shown in Fig. A.8 were generated loosely based on the lab experiment discussed in Section 3. Note that some of the parameter combinations, which were chosen for illustrative purposes, are close to or just beyond the limit of what could be considered physically reasonable. The aperture values are reported based on the narrow fracture assumption that $b_i = V_i/A_i$, although that may result in aperture values which are off by a factor of two, since the effective heat-transfer surface area for the square cross-section limit is $2V_i/b_i$.

References

Aksoy, N., Serpen, U., 2005. Reinjection management in Balcova geothermal field. In: Proceedings of the World Geothermal Congress 2005. Antalya, Turkey, pp. 1–11.

Aksoy, N., Serpen, U., Filiz, Ş., 2008. Management of the Balcova–Narlidere geothermal reservoir, Turkey. Geothermics 37 (4), 444–466. http://dx.doi.org/10.1016/j.geothermics.2007.12.003.

Axelsson, G., 2008. Importance of geothermal reinjection. In: Presented At the Workshop for Decision Makers on Direct Heating Use of Geothermal Resources in Asia. Tianjin, China, pp. 1–16.

Axelsson, G., Björnsson, G., Montalvo, F., 2005. Quantitative interpretation of tracer test data. In: Proceedings of the World Geothermal Congress 2005. Antalya, Turkey.

Axelsson, G., Flovenz, O.G., Hauksdottir, S., Hjartarson, A., Liu, J., 2001. Analysis of tracer test data, and injection-induced cooling, in the Laugaland geothermal field, N-Iceland. Geothermics 30 (6), 697–725. http://dx.doi.org/10.1016/S0375-6505(01)00026-8.

Berkowitz, B., Cortis, A., Dentz, M., Scher, H., 2006. Modeling non-Fickian transport in geological formations as a continuous time random walk. Rev. Geophys. 44 (2), RG2003. http://dx.doi.org/10.1029/2005RG000178.

Brown, D., DuTeaux, R., Kruger, P., Swenson, D., Yamaguchi, T., 1999. Fluid circulation and heat extraction from engineered geothermal reservoirs. Geothermics 28 (4–5), 553–572. http://dx.doi.org/10.1016/S0375-6505(99)00028-0.

Castagna, M., Becker, M.W., Bellin, A., 2011. Joint estimation of transmissivity and storativity in a bedrock fracture. Water Resour. Res. 47 (9), W09504. http://dx.doi.org/10.1029/2010WR009262.

Cherubini, C., Pastore, N., Giasi, C.I., Allegretti, N.M., 2017. Laboratory experimental investigation of heat transport in fractured media. Nonlinear Process. Geophys. 24 (1), 23–42. http://dx.doi.org/10.5194/npg-24-23-2017.

Co, C.K.D., Horne, R.N., 2011. Characterization of geothermal interwell connectivity using thermal and tracer data. GRC Trans. 35, 1411–1416.

Co, C.K.D., Horne, R.N., 2012. Coupled temperature and tracer data analysis using a uniform porous channel model. GRC Trans. 36, 1263–1268.

Egert, R., Gholami Korzani, M., Held, S., Kohl, T., 2020. Implications on large-scale flow of the fractured EGS reservoir Soultz inferred from hydraulic data and tracer experiments. Geothermics 84, 101749. http://dx.doi.org/10.1016/j.geothermics.2019.101749.

Fridleifsson, G.O., Ármannsson, H., Mortensen, A.K., 2006. Geothermal conditions in the Krafla caldera with focus on well KG-26. A review in relation to the Iceland Deep Drilling Project. Technical Report ÍSOR–2006/030, Iceland Geosurvey.

Geng, J., Sun, Q., Zhang, Y., Cao, L., Lü, C., Zhang, Y., 2018. Temperature dependence of the thermal diffusivity of sandstone. J. Pet. Sci. Eng. 164, 110–116. http://dx.doi.org/10.1016/j.petrol.2018.01.047.

Goranson, R.W., 1942. Heat capacity; heat of fusion. In: Birch, A.F., Schairer, J.F., Spicer, H.C. (Eds.), Handbook of Physical Constants, vol. 36. Geological Society of America, ISBN: 9780813720364, pp. 235–236. http://dx.doi.org/10.1130/SPE36-p223.

Gringarten, A.C., Sauty, J.P., 1975. A theoretical study of heat extraction from aquifers with uniform regional flow. J. Geophys. Res. 80 (35), 4956–4962. http://dx.doi.org/10.1029/JB080i035p04956.

Hawkins, A.J., Becker, M.W., Tester, J.W., 2018. Inert and adsorptive tracer tests for field measurement of flow-wetted surface area. Water Resour. Res. 54 (8), 5341–5358. http://dx.doi.org/10.1029/2017WR021910.

Hawkins, A.J., Fox, D.B., Becker, M.W., Tester, J.W., 2017. Measurement and simulation of heat exchange in fractured bedrock using inert and thermally degrading tracers. Water Resour. Res. 53 (2), 1210–1230. http://dx.doi.org/10.1002/2016WR019617.

Hawkins, A.J., Fox, D.B., Koch, D.L., Becker, M.W., Tester, J.W., 2020. Predictive inverse model for advective heat transfer in a short-circuited fracture: Dimensional analysis, machine learning, and field demonstration. Water Resour. Res. 56 (11), http://dx.doi.org/10.1029/2020WR027065, e2020WR027065.

Horne, R.N., 1982. Effects of water injection into fractured geothermal reservoirs : a summary of experience worldwide. http://dx.doi.org/10.2172/860855.

Ikhwanda, F., Suzuki, A., Hashida, T., 2018. Development of numerical methods for estimating fluid flow path in fractured geothermal reservoir. In: Proceedings of the 43rd Workshop on Geothermal Reservoir Engineering. Stanford, CA: Stanford University, pp. 1–11.

Jacobsen, R.T., Lemmon, E.W., Penoncello, S.G., Shan, Z., Wright, N.T., 2003. Thermophysical properties of fluids and materials. In: Bejan, A., Kraus, A.D. (Eds.), Heat Transfer Handbook. John Wiley & Sons, p. 138.

Kaya, E., Zarrouk, S.J., O'Sullivan, M.J., 2011. Reinjection in geothermal fields: A review of worldwide experience. Renew. Sustain. Energy Rev. 15 (1), 47–68. http://dx.doi.org/10.1016/j.rser.2010.07.032.

Kittilä, A., Jalali, M., Saar, M.O., Kong, X.Z., 2020. Solute tracer test quantification of the effects of hot water injection into hydraulically stimulated crystalline rock. Geotherm. Energy 8 (1), 17. http://dx.doi.org/10.1186/s40517-020-00172-x.

Lauwerier, H.A., 1955. The transport of heat in an oil layer caused by the injection of hot fluid. Appl. Sci. Res. 5 (2–3), 145–150. http://dx.doi.org/10.1007/BF03184614.

Mora, Y.T., Torres, H.F., 2013. Geochemical characterization and integral analysis of data Las Pailas geothermal field, Costa Rica. In: Presented at Short Course V on Conceptual Modelling of Geothermal Systems. Santa Tecla, El Salvador, pp. 1–10.

Oliver, D.S., 2017. Metropolized randomized maximum likelihood for improved sampling from multimodal distributions. SIAM/ASA J. Uncertain. Quant. 5 (1), 259–277. http://dx.doi.org/10.1137/15M1033320.

Oliver, D.S., He, N., Reynolds, A.C., 1996. Conditioning permeability fields to pressure data. In: Proceedings of the 5th European Conference on the Mathematics of Oil Recovery. Leoben, Austria, pp. 259–270. http://dx.doi.org/10.3997/2214-4609.201406884.

OpenSCAD, 2021. The programmers solid 3D CAD modeller. [Online] https://www.openscad.org/. (Accessed 28 September 2021).

Pastore, N., Cherubini, C., Giasi, C.I., Allegretti, N.M., Redondo, J.M., Tarquis, A.M., 2015. Experimental study of heat transport in fractured network. Energy Procedia 76, 273–281. http://dx.doi.org/10.1016/j.egypro.2015.07.860.

Reimus, P., Caporuscio, F., Marina, O., Janney, D., 2020. Field demonstration of the combined use of thermally-degrading and cation-exchanging tracers to predict thermal drawdown in a geothermal reservoir. Geothermics 83, 101712. http://dx.doi.org/10.1016/j.geothermics.2019.101712.

Rivera Diaz, A., Kaya, E., Zarrouk, S.J., 2016. Reinjection in geothermal fields — A worldwide review update. Renew. Sustain. Energy Rev. 53, 105–162. http://dx.doi.org/10.1016/j.rser.2015.07.151.

Robertson, E.C., 1988. Thermal properties of rocks. Open-File Report 88–441, United States Geological Survey, Reston, Virginia.

Robinson, B.A., Tester, J.W., 1984. Dispersed fluid flow in fractured reservoirs: An analysis of tracer-determined residence time distributions. J. Geophys. Res. 89 (B12), 10374–10384. http://dx.doi.org/10.1029/JB089iB12p10374.

Rose, P.E., Benoit, W.R., Kilbourn, P.M., 2001. The application of the polyaromatic sulfonates as tracers in geothermal reservoirs. Geothermics 30 (6), 617–640. http://dx.doi.org/10.1016/S0375-6505(01)00024-4.

Rose, P.E., Mella, M., Kasteler, C., Johnson, S.D., 2004. The estimation of reservoir pore volume from tracer data. In: Proceedings of the 29th Workshop on Geothermal Reservoir Engineering. Stanford University, Stanford, CA, pp. SGP–TR–175.

Sanjuan, B., Pinault, J.-L., Rose, P., Gérard, A., Brach, M., Braibant, G., Crouzet, C., Foucher, J.-C., Gautier, A., Touzelet, S., 2006. Tracer testing of the geothermal heat exchanger at Soultz-sous-Forêts (France) between 2000 and 2005. Geothermics 35 (5–6), 622–653. http://dx.doi.org/10.1016/j.geothermics.2006.09.007.

Seymour, J.D., Callaghan, P.T., 1997. Generalized approach to NMR analysis of flow and dispersion in porous media. AIChE J. 43 (8), 2096–2111. http://dx.doi.org/10.1002/aic.690430817.

Shook, G.M., Suzuki, A., 2017. Use of tracers and temperature to estimate fracture surface area for EGS reservoirs. Geothermics 67, 40–47. http://dx.doi.org/10.1016/j.geothermics.2016.12.006.

Stefánsson, V., 1997. Geothermal reinjection experience. Geothermics 26 (1), 99–139. http://dx.doi.org/10.1016/S0375-6505(96)00035-1.

Suzuki, A., 2017. Estimation of fracture surface area based on tracer and temperature histories. GRC Trans. 41, 2865–2879.

Suzuki, A., Ikhwanda, F., Yamaguchi, A., Hashida, T., 2019a. Estimations of fracture surface area using tracer and temperature data in geothermal fields. Geosciences 9 (10), 425. http://dx.doi.org/10.3390/geosciences9100425.

Suzuki, A., Minto, J.M., Watanabe, N., Li, K., Horne, R.N., 2019b. Contributions of 3D printed fracture networks to development of flow and transport models. Transp. Porous Media 129 (2), 485–500. http://dx.doi.org/10.1007/s11242-018-1154-7.

Suzuki, A., Niibori, Y., Fomin, S.A., Chugunov, V.A., Hashida, T., 2015. Analysis of water injection in fractured reservoirs using a fractional-derivative-based mass and heat transfer model. Math. Geosci. 47, 31–49. http://dx.doi.org/10.1007/s11004-014-9522-5.

Suzuki, A., Watanabe, N., Li, K., Horne, R.N., 2017. Fracture network created by 3-D printer and its validation using CT images. Water Resour. Res. 53 (7), 6330–6339. http://dx.doi.org/10.1002/2017WR021032.

Tsoflias, G.P., Becker, M.W., 2008. Ground-penetrating-radar response to fracture-fluid salinity: Why lower frequencies are favorable for resolving salinity changes. Geophysics 73 (5), J25–J30. http://dx.doi.org/10.1190/1.2957893.

Tsoflias, G.P., Perll, C., Baker, M., Becker, M.W., 2015. Cross-polarized GPR imaging of fracture flow channeling. J. Earth Sci. 26 (6), 776–784. http://dx.doi.org/10.1007/s12583-015-0612-1.

Vogt, C., Marquart, G., Kosack, C., Wolf, A., Clauser, C., 2012. Estimating the permeability distribution and its uncertainty at the EGS demonstration reservoir Soultz-sous-Forêts using the ensemble Kalman filter. Water Resour. Res. 48 (8), W08517. http://dx.doi.org/10.1029/2011WR011673.

Wu, H., Fu, P., Hawkins, A.J., Tang, H., Morris, J.P., 2021. Predicting thermal performance of an enhanced geothermal system from tracer tests in a data assimilation framework. Water Resour. Res. 57 (12), http://dx.doi.org/10.1029/2021WR030987, e2021WR030987.